The full-length prototype of the KLOE drift chamber

A. Andryakov[a,1], C. Avanzini[b,2], C. Bacci[c], H. Beker[b,3], G. Bencivenni[a], L. Bucci[a],
G. Cataldi[d,4], F. Ceradini[c], P. Creti[d], E. De Lucia[b], A. Denig[e], P. De Simone[a], F. Donno[a,5],
V. Elia[d], G. Felici[a], G. Finocchiaro[a], V. Golovatyuk[d,6], E. Gorini[d], F. Grancagnolo[d],
W. Grandegger[a,7], U. vonHagel[e], W. Kluge[e], F. Lacava[b], C. Luisi[b], G. Margutti[b,8],
R. Messi[f], M. Panareo[d], L. Paoluzi[f], E. Pasqualucci[f,9], V. Patera[a], D. Picca[b],
L. Pontecorvo[b], M. Primavera[d], S. Spagnolo[d,*], P. Valente[a,10]

[a] Laboratori Nazionali di Frascati dell'INFN, Frascati, Italy
[b] Dipartimento di Fisica dell'Università "La Sapienza" and INFN, Roma I, Italy
[c] Dipartimento di Fisica dell'Università Roma Tre and INFN, Roma I, Italy
[d] Dipartimento di Fisica dell'Università and INFN, Lecce, Italy
[e] Institut für Experimentelle Kernphysik, Universität Karlsruhe, Germany
[f] Dipartimento di Fisica dell'Università "Tor Vergata" and INFN, Roma II, Italy

Received 14 October 1997

Abstract

The main goal of the KLOE experiment is the study of CP violation in the K mesons system, with an accuracy of 10^{-4} in the measurement of $Re(\varepsilon'/\varepsilon)$. This task imposes strong constraints on the design and operation of the drift chamber, which must reconstruct the charged decays of low momentum K_L's and K_S's with high efficiency and high resolution. A full-length prototype of the chamber has been built and tested on a 50 GeV/c beam. The analysis of the large sample of data has allowed a detailed study of the time to distance relations as a function of the track parameters and of the peculiar geometry of the drift cell. The detector performance, in terms of efficiency, spatial resolutions and dE/dx resolution, is illustrated and discussed. © 1998 Elsevier Science B.V. All rights reserved.

* Corresponding author.
[1] Present address: ITEP, Moskow.
[2] Presently at ALENIA Spazio, Roma, Italy.
[3] Present address: CERN, Geneva, Switzerland.
[4] Present address: Institut für Experimentelle Kernphysik, Universität Karlsruhe, Germany.
[5] Present address: Sezione INFN, Pisa, Italy.
[6] On leave from JINR, Dubna, Russia.
[7] Presently at CES Creative Electronic Systems SA, Switzerland.
[8] Presently at Texas Instruments, Avezzano, Italy.
[9] Now at Laboratori Nazionali di Frascati dell'INFN, Frascati, Italy.
[10] Presently at Dipartimento di Fisica dell'Università "Tor Vergata" and INFN, Roma II, Italy.

1. Introduction

The detector of the KLOE experiment [1] at the DAΦNE ϕ factory in Frascati has been designed primarily with the goal of detecting direct CP violation in K^0 decays with a sensitivity of 10^{-4} in $Re(\varepsilon'/\varepsilon)$. It consists (see Fig. 1) of a cylindrical drift chamber and a hermetic electromagnetic calorimeter inside of a solenoidal superconducting magnet, providing a field of 0.6 T.

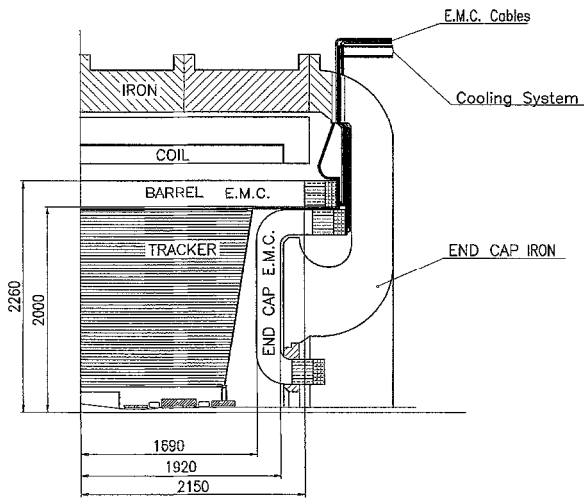The most demanding task for the tracking chamber [2–4] is the detection and the reconstruction of

Fig. 1. Vertical cross section of 1/4 of the KLOE detector.

the $K_L \to \pi^+\pi^-$ decays, in particular the precise localization of the decay vertices which affects the determination of the number of events belonging to the fiducial volume. The required vertex resolution is 1 mm. A large, highly homogeneous and isotropic active volume is also required because of the average decay length (~ 350 cm) of the K_L and of the uniform distribution of their decay vertices and products. Moreover, a reasonable compromise must be reached between a good granularity, in order to achieve a high and well-controlled efficiency and to maximize the fiducial volume, and a high transparency, in order to keep the multiple scattering (the $\pi^\pm$ momentum spectrum from $K_L \to \pi^+\pi^-$ is essentially flat between 140 and 270 MeV/c and for $K_L \to \pi^+\pi^-\pi^0$ the average $\pi^\pm$ momentum is only 130 MeV/c), the K_S regeneration effects and the total number of wires, and therefore of electronics channels, within acceptable limits. These considerations have led to the design of a cylindrical drift chamber of 4 m diameter and 3.2 m length (at the outer radius), in which 12 582 single sense wire, almost square shaped cells are arranged in 58 circular layers. The "all-stereo" wire configuration ensures the highest uniformity in filling the sensitive volume. Consecutive layers have stereo angles of opposite signs. The inward radial displacement at the chamber center (stereo drop) is

fixed to 1.5 cm for all layers, in order to better preserve the cell shape along the chamber radius. The resulting stereo angles increase with the layer radius from ± 60 to ± 150 mrad. The cell size, defined with a 3:1 field to sense wires ratio, is $2 \times 2\pi/3$ cm^2 for the 12 inner layers, for better tracking and vertexing of the $K_S \to \pi^+\pi^-$ decays, and $3 \times \pi$ cm^2 for the following 46 layers. The chamber mechanical structure is based on large Young modulus and very transparent materials, to minimize both the deformations due to the total load of the wires (~ 3.5 t) and the thickness in terms of X_0. The two end plates, made of 9 mm thick quasi-isotropic carbon fiber, spherical with 10 m radius of curvature, are kept apart by 12 rods of unidirectional carbon fiber, attached to the end plates via a carbon fiber outer flange. The spherical shape of the end plates minimizes their deformation under axial load.

The choice of the gas is innovative: a helium-based gas mixture is adopted, in order to minimize multiple scattering, photon conversion before the calorimeter and K_S regeneration effects inside the active volume. Moreover, the low drift velocity [5,6] and, consequently, the small distortions due to the Lorentz angle, and the small diffusion [7], allow for good spatial resolution. A quite satisfactory mixture, as far as resolution, efficiency and operating conditions are concerned, is 90–10% He–iC$_4$H$_{10}$, with a radiation length $X_0 = 1300$ m [8].

For expected spatial resolutions of $\sigma_{r\phi} \sim 200$ μm and $\sigma_z \sim 2$ mm on a single measurement, one gets a transverse momentum resolution of better than 0.5% with a resulting di-pion invariant mass resolution of the order of ~ 1 MeV/c^2.

Given the complexity of the drift chamber design, and the novelty of many solutions adopted by KLOE, a full-length prototype of the chamber has been built in Lecce [4,9], in order to test both the performance of the "all-stereo" geometry and the helium-based gas mixture, and to acquire first-hand experience about all problems concerning materials, stringing procedures and gas tightness. The prototype operation has been first monitored with cosmic rays and then with a beam test run done at CERN, in order to analyze its performance in different working configurations and to obtain

a complete set of calibration constants. In the following sections, a detailed description of the prototype and of the beam test layout are presented, then the performances of the prototype, as far as resolutions (spatial, angular, momentum and dE/dx) and efficiencies are concerned, are analyzed and discussed.

2. The full-length prototype

2.1. Mechanical description

The full-length prototype [9,10] of the KLOE drift chamber has the shape of a cylindrical sector, with inner radius of 25 cm, outer radius of 109 cm and length at inner radius of 290 cm. The two end-plates, portions of a conical surface, have a half aperture angle of 80° and an angle of the conical sector of 90°. They are 6.2 mm thick, made of almost isotropically laminated layers of prepreg T300-type carbon fiber [11], covered, on both sides, by a 37 μm gold-plated copper foil (in order to electrically shield the chamber and to ease the soldering of the field wires to ground). The lateral surfaces of the detector consist of two cylindrical sectors and two flat surfaces of 3 mm thick aluminum, reinforced along the perimeter with glued aluminum bars of $20 \times 30\,mm^2$ cross section. Both end-plates and the closing surfaces are fixed on a reticular aluminum frame of $50 \times 50\,mm^2$ cross section. A rubber gasket, inserted between the panels and the frame, ensures good gas tightness. About 500 tungsten sense wires, 25 μm diameter, and 1800 aluminum field and guard wires, 80 μm diameter, are strung in the chamber with a mechanical tension of, respectively, 65 and 100 g, corresponding to an average gravitational sagitta of 250 μm. These are pneumatically crimped inside, respectively, copper and aluminum feedthroughs, embedded in delrin, which is molded around them and press-fit onto the end plates. Gas leaks from the feedthrough holes are avoided by sealing the holes with a microdrop dispensed viscousless sealant (Loctite 420). The wire stringing was done inside a class 10 000 clean room to prevent possible contaminations. A schematic view of the prototype is shown in Fig. 2. The internal structure consists of
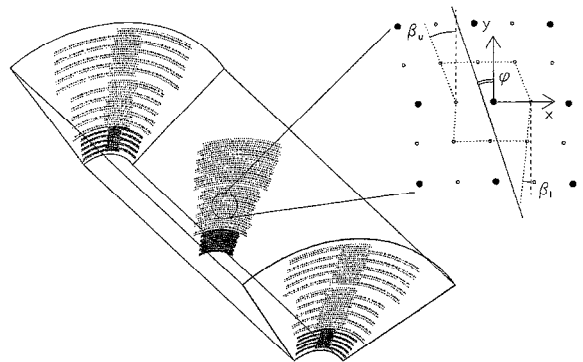

Fig. 2. View of the prototype showing the position of the wires at the two end plates and at the center. The inset shows a cross section of a cell with the definition of the parameters ϕ, β_ℓ and β_u (see Section 2.3). Larger dots represent sense wires.

480 single sense wire square cells, arranged in 30 circular and coaxial layers strung at stereo angles of alternating sign. The value of the stereo angles increases approximately with the square root of the layer radius.

2.2. Layer structure

From the point of view of the layer geometry, the drift chamber prototype is separated into three different regions:

1. the innermost 10 layers, with cells of $(1.5 \times \pi/2)\,cm^2$ size, as opposed to $(2 \times 2\pi/3)\,cm^2$ as in the KLOE chamber, and stereo angles in the range from 50–60 mrad, corresponding to a stereo drop (the inward radial displacement at the center of the wire) $\delta = 1\,cm$;
2. a middle region, with 10 layers of $(3 \times \pi)\,cm^2$ cells, stereo angles between 60 and 80 mrad and $\delta = 1\,cm$;
3. the outermost 10 layers, with cell size of $(3 \times \pi)\,cm^2$ and stereo drop of $\delta = 2\,cm$, with corresponding stereo angles in the range 115–130 mrad, in order to simulate, at a smaller radius, the stereo angle configuration of the outer layers of the KLOE chamber (see Fig. 2).

At the boundary between the two sections with different stereo drops, and at the innermost and

outermost radii of the prototype, layers of guard wires ensure a good gas gain uniformity.

Because of the large value of the stereo angles, only for a limited region of the cylindrical sector there exists a considerable overlap of layers with closed cells. This overlapping region extends, however, over the full length of the prototype, from a minimum of 6 cells at the end plates up to a maximum of 17 cells at the center (Fig. 2).

2.3. Cell structure

The KLOE drift chamber cell is a single sense wire cell. Its cross section appears, in a plane perpendicular to the chamber axis at the center ($z = 0$ plane), like a slightly deformed square (see inset in Fig. 2). While a special choice of the stereo angle values has allowed us to keep constant the cell radial dimension along the chamber axis (the relative variations are below 0.3%), a small increase of the cell width, from the middle of the chamber towards the end plates, of the order of a few percent, is produced by the stereo arrangement.

The three field wires which define the inner radial side of the cell and the two lateral field wires are almost parallel and symmetric with respect to the sense wire. Counterwise, the field wires at the outer side in one layer belong, by construction, to the successive layer, both in their number and in their stereo angle (value and sign). This produces two kinds of effects: (1) in any plane perpendicular to the z-axis, the relative positions of the sense wire and of the field wires at the outer side of the cells change cell by cell; (2) for each cell these relative positions change periodically along z. As a consequence, the outer half part of the cell is affected by a non-negligible z-dependent deformation, with respect to a square shape, which can be parameterized by means of the angle β_u shown in the inset in Fig. 2.

A second-order effect is due to the small difference between the values of the stereo angle of the sense wire and of field wires at the inner side (of the order of 1 mrad) which produces a slight shift of the base of the cell, at the end plates, on one side or the other, according to the sign of the stereo angle. This deformation, parameterized by the angle β_f, increases monotonically (almost linearly) with z.

3. Beam test layout

The prototype has been tested [3,10] with the SPS T1-X7 beam in the West Area of CERN. In Fig. 3 the schematic layout of the experimental setup is shown. The beam consisted of 50 GeV/c positive pions, with a small contamination of positrons. The beam profile was symmetric and approximately Gaussian with $\sigma = 1.5$ cm in the vertical plane and $\sigma = 2.5$ cm in the horizontal plane. It could be defocussed to double its dimensions in both planes. The maximum number of particles was of 1.3×10^3 during the spill time (2.37 s), in each SPS working cycle of 14.4 s.Two pairs of crossed scintillators, placed upstream and downstream of the prototype, provided a beam trigger with a four-fold coincidence. The trigger rate was of the order of 0.7×10^3 Hz and its jitter was contained within 1–2 ns. The prototype was anchored to a movable stand, capable of rotating around a longitudinal axis and around an axis perpendicular to this and to the beam direction, with a precision of a few degrees, and of translating along the two directions orthogonal to the beam, with a precision of a few centimeters. An optical system, consisting of a He–Ne laser, mirrors and positioning stages, was used to align the prototype frame at the required orientations, with respect to the beam, by means of appropriate mylar windows placed on the detector. All movements were remotely controlled and did not require beam interruption during data taking.

A total number of 27×10^6 events, taken during one week of beam time, was written on tape for different values of high voltage on sense and guard wires and for different values of discriminator thresholds, to study chamber efficiency, noise and cross-talk effects.

The prototype orientation with respect to the beam direction was changed from a configuration in which the beam crossed the chamber radially, to orientations where the chamber was translated and rotated in both polar and azimuthal angles, in order to illuminate the prototype cells at different positions along the wires and at all possible angles. Few special dedicated runs were also taken, during which the gas flow rate was changed by a factor 4, in order to check the stability of the gas mixture against possible contaminations due to gas leaks.
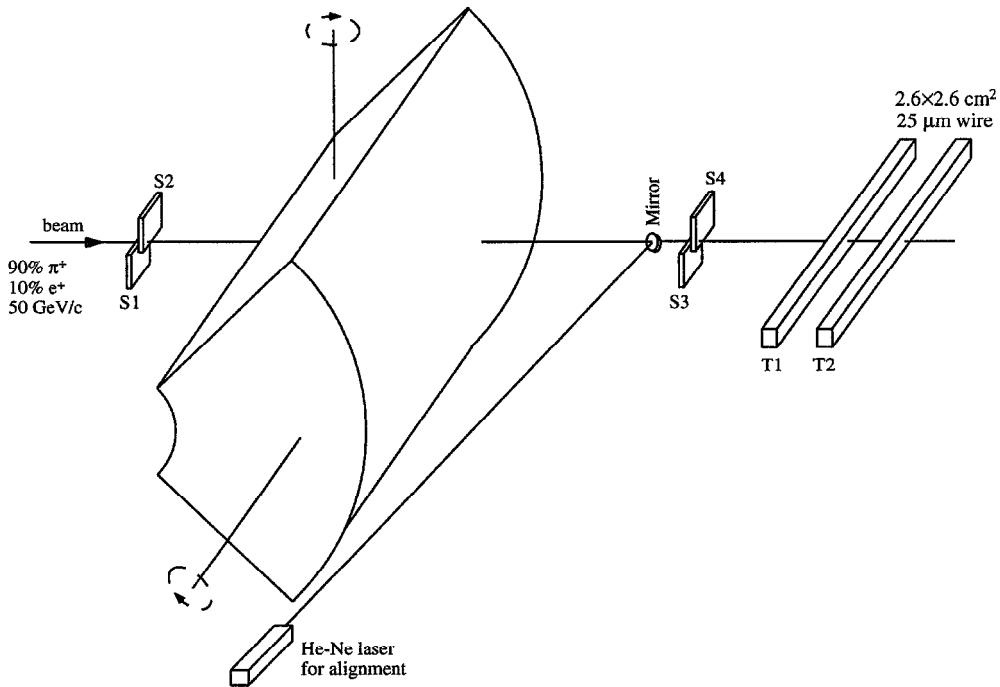
Fig. 3. Schematic layout of the beam test.

3.1. HV and frontend electronics

The sense wires were kept at positive voltage of about 2000 V by means of a remotely controlled high-voltage power supply (CAEN SY127). The high-voltage was filtered and sent to distribution boxes situated on one end. Each channel from the boxes supplied 6 or 12 wires groups by means of distribution cards. The field wires were individually soldered to ground on the gold-plated end plate.

The preamplifier cards, instrumented with the VTX chip from Tektronix [12], were mounted on the other end plate. This chip is characterized by a very high gain of 1.0 mV/fC on 50 Ω and a rise time of 5 ns. It was chosen for the final configuration of the chamber because of its extremely low-power dissipation, about 10 mW/channel, and low total mass.

Approximately one-half of the sense wires were left floating on the side opposite to the preamplifier and the rest were terminated to ground on their characteristic impedance ($\sim$ 390 Ω) to investigate

possible differences on time and amplitude digitization. No differences were found on time or amplitude resolutions. The signals from the preamplifiers were sent to the post-amplifier discriminators housed in VME 9U cards; each card was able to process 48 channels and gave two outputs: one for the TDC and the other for the ADC. The drift time of 480 cells was read out with commercial TDCs (LeCroy mod. 2277, 1 ns resolution) in common start mode and 74 of the innermost cells were read also by ADCs (LeCroy 2249W and CAEN C205A).

3.2. Data acquisition and monitoring system

A standard DAQ system developed for the KLOE beam tests [13] was used to read the data. Two CAMAC crates were interfaced to a VME crate on a single VIC bus. The readout was performed on a 68030 VME processor (FIC 8234 from CES), where a real-time UNIX system, LynxOS, was running. The acquisition process was controlled by a graphical user interface under X Windows and

Tcl/Tk [14]. During a burst, the data were read out by the processor and stored in its internal memory, then they were transferred over the network to a workstation DEC 3000/400, where the run control process was executing, writing the events and the run conditions on exabyte cassettes and making the data accessible to the on-line monitoring program in order to extract efficiencies, noise, ADC and TDC distributions, to give a real-time detailed performance of the detector.

3.3. Gas system

During the beam test, the gas system was operating in open regime, the gas mixture was set by means of mass flowmeters and the gas flow was monitored by flow controllers. Pressures, temperature and humidity were also monitored. Temperature was fairly constant during the whole beam test. Pressure corrections were applied for dE/dx studies. Two external proportional tubes (T1 and T2), $2.6 \times 2.6\,cm^2$ cross-sectional area, instrumented with the same sense wire (25 μm diameter gold-plated W) and the same electronic chain as the prototype, at the same nominal gas gain, were placed on the beam line downstream of the prototype to monitor the gas mixture in the chamber: T1 was connected in parallel to the chamber gas inlet, while T2 was connected in series downstream of the gas chamber. Small differences in the

pulse integral distributions and in the drift time distributions between the two tubes would suggest possible gas contamination due to gas leaks in the prototype. Accurate analysis of these distributions, after appropriately swapping of T1 and T2, of their electronic chains and of their gas suppliers, has shown that, even at the lowest flow rate corresponding to 1 volume ($\sim 3\,m^3$) change per day, no appreciable gas contamination was present in the gas downstream of the prototype [15]. This result is a good indication that sealing of the feedthrough holes was very effective in preventing possible gas leaks.

3.4. Operating conditions

The gas mixture used was 90% helium–10% isobutane, at a flow rate corresponding to about 2 volume changes per day. We shall concentrate our attention to $3 \times \pi\,cm^2$ cells only with properly terminated sense wires on the side opposite to the preamplifiers. Analogous and equivalent results hold for unterminated cells and for $1.5 \times 2\pi/3\,cm^2$ cells. Fig. 4a shows the layer efficiency plateau, for different values of the equivalent threshold at the signal level, and for normal incidence tracks. The corresponding average hit cell multiplicity per layer is shown in Fig. 4b.

The chosen operating voltages were 1950 V with an equivalent threshold of 4 mV at the preamplifier
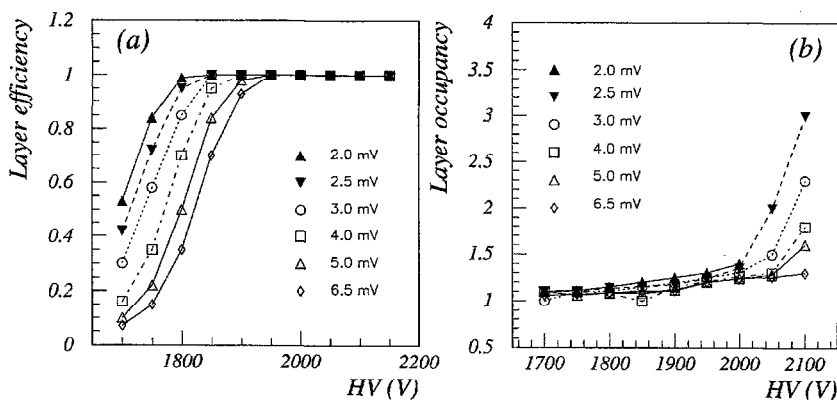

Fig. 4. (a) Efficiency plateau for $(3 \times \pi)\,cm^2$ cells. (b) Average hit multiplicity per layer for different values of threshold. HV is the high voltage on the sense wire.

input and 1900 V with 2.5 mV, where most of the data were taken (1750 and 1700 V for small cells). It is worth noticing that, even at the lowest value of threshold (2 mV), full efficiency on the whole system is reached at a HV corresponding to an average hit cell multiplicity of the order of 1.2. At 1950 V, a single electron gives an average pulse height of 16 mV, consistent with a gas gain of approximately 10^5.

4. Time to distance relations

One of the main motivations for building this prototype was the possibility of studying the cell response in the real environment of the tracking detector, in order to reproduce closely all its peculiar features. The need for this study comes from the special topology of the cell, complicated by the global geometry of the chamber. The dependence of the transport parameters from the magnetic field has been studied with a small prototype [16].

The response of the KLOE cell is primarily affected by its square shape and by the discrete cathodic edge.

The square cell shape entails a dependence of the time to distance relations on the angle ϕ that the particle trajectory makes with the y-axis in the local cell reference frame (for the definition of angles and reference frame see inset in Fig. 2).

In the simplifying hypotheses of an "ideal" square cell, the time to distance relations, $r(t_d)$, depend on the track angle ϕ with respect to the cell axis but must obey to the symmetries:

$$r(t_d; \phi) = r(t_d; -\phi), \qquad (1)$$

$$r(t_d; \pi/4 - \phi) = r(t_d; \pi/4 + \phi). \qquad (2)$$

Actually, as already pointed out in Section 2.3, the floating position of the outer field wires produces a deformation of the outer-half of the drift area. As a consequence, the β_u angle affects the $r(t_d)$ function in a different way for each value of the track angle ϕ, thus spoiling the cell symmetry. The residual approximate symmetry one can still assume valid in the outer-half-cell is

$$r(t_d; \phi, \beta_u) = r(t_d; -\phi, -\beta_u), \qquad (3)$$

while the symmetries in Eqs. (1) and (2) hold in the inner-half-cell because of the very low value of the β_ℓ angle.

4.1. Determination of t_0

Before the study of the parameterization of the impact parameter as a function of the measured drift time can be attempted, it is necessary to obtain the time offset, t_0, for all wires. For this purpose, one looks at the raw distribution of the drift times: t_0 is defined as the inflection point of the rising edge of this distribution and corresponds to the case of a track with null impact parameter. It can be shown that the derivative of the time distribution can very well be approximated to a Gaussian with a mean value corresponding to the inflection point and a sigma corresponding to the time resolution of the cell. A study of t_0 as a function of the z coordinate of the beam impact point on the chamber for the same wires, at normal incidence, allows to infer the value of the transmission velocity of the signal, $v^{-1} = (4.1 \pm 0.2)$ ns/m, which represents an important correction to the track fit, given the considerable length of the chamber. Stability of the t_0 values was monitored throughout the duration of the test and, in order to minimize the number of corrections to the track fit, due to time of flight, transit time and angle of beam, a set of t_0 values was calculated and used for each configuration.

A typical raw time distribution for a cell with its derivative is shown in Fig. 5; the inset shows the region of the time scale corresponding to the Gaussian distribution for t_0.

4.2. Parameterization of the impact parameter

In the beam test, the prototype has been used as a self-tracking device (i.e., no external hodoscope was used) and a special algorithm, described in detail elsewhere [17], for straight track reconstruction in the all stereo geometry (for which the pattern recognition task is not trivial) was applied to the analysis of the data sample. The impact parameter of the track in a given cell is measured by fitting all the remaining hits in the track to a straight line and by computing the distance of
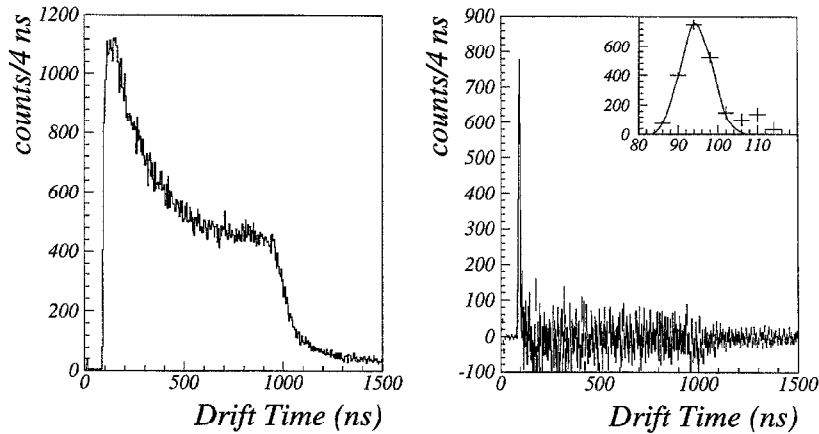
Fig. 5. Raw time distribution of a single cell. The inset shows the Gaussian fit to the peak, corresponding to t_0, of the distribution of the time derivative.

closest approach of the reconstructed track to the sense wire. The correlation between impact parameter and drift time, $r(t_d)$, is extracted with a quickly converging iterative procedure: a rough estimate of the time to distance relation is used to get the first approximation of the track trajectory which allows us to compute a second-order approximation of $r(t_d)$ to be used as more refined input for the track-fitting algorithm. Usually, two iterations of the procedure provide a stable determination of $r(t_d)$.

In the case of tracks crossing the detector at $\phi = 0$ and in the plane $z = 0$, for which β_ℓ and β_u are not relevant, $r(t_d)$ is parameterized by three-fourth order polynomials, connected at $t_d = 450$ ns (approximately one-half of the half cell width, $w/2$), where $r(t_d)$ is continuous and differentiable, and at $t_d = 880$ ns ($\sim 90\%$ of $w/2$), where only the function continuity is demanded (see Fig. 6a). Here, as well as in the following, we refer, without loss of generality, to the $3 \times \pi\,\mathrm{cm}^2$ cells, where a slightly lower average drift velocity, 1.6 cm/μs compared to 2.1 cm/μs in the smaller cells, enhances the edge and anisotropy effects.

While the first branch polynomial is independent of ϕ, β_ℓ and β_u, the anisotropy and the cell deformations affect $r(t_d)$ at impact parameters larger than 1 cm ($\sim 2/3$ of $w/2$) by amounts much larger than the resolution. In order to disentangle the

different effects, the hits have been, firstly, grouped in discrete ranges of the ϕ angle and then, within each of these, in discrete values of β_u and β_ℓ.[11] The width of the different ϕ ranges has been chosen such as to keep constant, and roughly equal to the average chamber resolution, the difference in $r(t_d)$ for two consecutive ranges.

Since $|\beta_\ell| < 9°$, two sets of curves ($\beta_\ell > 0$ and $\beta_\ell < 0$) in each ϕ range are enough to describe the cell behavior in its inner part. In the cell outer-half, β_u ranges from $-30°$ and $+30°$ and, hence, the parameterization of $r(t_d)$ is split in a number of β_u ranges, increasing with $|\phi|$ from 1 up to 7, within each ϕ range. Fig. 7 shows the time to distance relations, in the inner part of the cell, corresponding to the different ϕ ranges both for the case $\beta_\ell > 0$ and for the case $\beta_\ell < 0$. In Fig. 8 the time to distance curves related to the different β_u ranges, in the ϕ range $25 - 40°$ (Fig. 8a) and $40 - 50°$ (Fig. 8b) where the cell deformation effect is large, are plotted. By exploiting the cell symmetries, a total number of 36 parameterizations of $r(t_d)$, coupled to the corresponding resolution functions $\sigma(t_d)$,

---

[11] Actually, in the prototype, the inner-half of the cell is square not in the plane $z = 0$, like in the KLOE drift chamber, but on one end plate. Therefore, at $z = 0$, β_ℓ acquires a value different from zero for every layer and of alternating sign from one layer to the next.
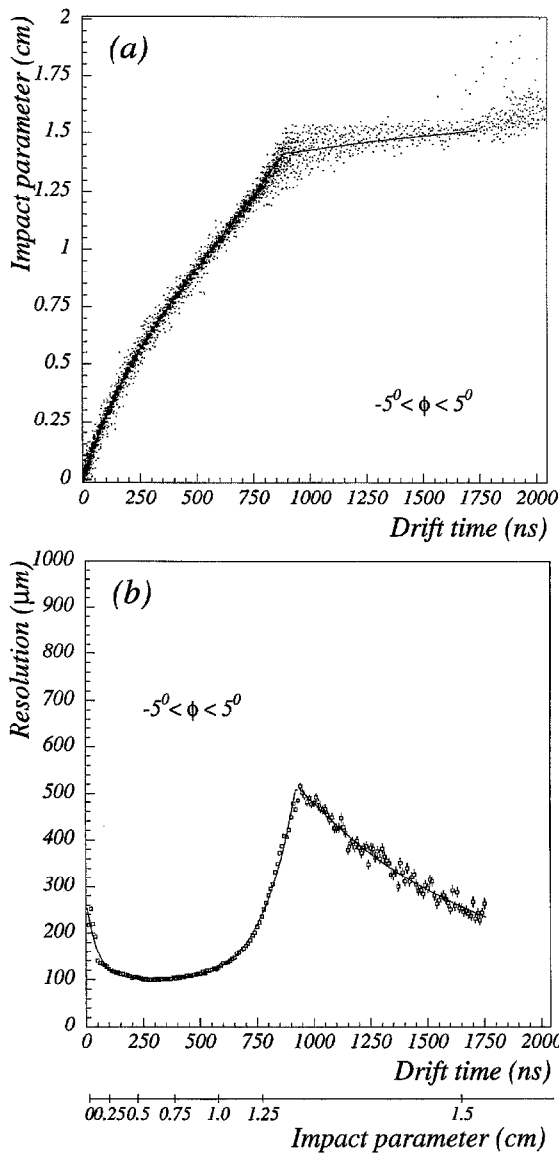
Fig. 6. Impact parameter as a function of the drift time for a $3 \times \pi \, cm^2$ cell crossed radially ($\phi = 0°$) (a). The fitting function described in the text is superimposed to the experimental points. For the same kind of tracks the resolution as a function of the

4.3. Parameterization of resolution

A similar iterative procedure adopted for obtaining the parameterization of the time to distance relation has been applied to the study of the relationship between drift time and resolution, $\sigma(t_d)$, as a function of the relevant parameters, ϕ, β_ℓ and β_u. The resolution has been evaluated in each bin of drift time[12] as the sigma of a Gaussian fit to the distribution of the differences $\Delta r(t_d)$ between the drift distance, measured by means of $r(t_d)$, and the reconstructed impact parameter. In the domain of short drift times, instead, for tracks very close to the sense wire, the quite low ionization density produces, besides of an increase of the average resolution, a systematic overestimate of the distance of closest approach. In these cases, this shift has been quadratically added to the RMS of the $\Delta r(t_d)$ distribution in order to get a more realistic estimate of the total resolution.

Fig. 6b shows the fit to the experimental data for tracks crossing the cell radially in the plane $z = 0$. The sharp increase of the resolution at drift times $t_d > 700 \, ns$, corresponding to impact parameters $> 1.15 \, cm$ (notice the strong non-linearity of the impact parameter scale at the bottom of the picture), is related to the proximity of the track to the field wire at the edge of the cell. The ionization electrons liberated near the cathodic lateral wires feel a radial electric field higher than that in the middle of the drift area. This produces two kinds of effects: a slight increase of the drift velocity, which entails the change in sign of the second derivative of the time to distance relation (just before the sharp knee in $r(t_d)$, shown in Fig. 6a) and a large spread of the arrival times of the fastest electron for a given impact parameter (last branch of the $r(t_d)$ function). This second effect arises from the large difference in the length of the drift paths starting radially around the field wire, enhanced by the large mean-free path for primary ionization in helium which allows the first electron to be generated in sites corresponding to quite different drift lines. For impact parameters

has proven to provide a complete and satisfactory description of the drift cell behavior. Table 1 summarizes the main features of the $r(t_d)$ parameterization in the different ϕ ranges considered.

---

[12] The width of the time bins, 10 or 15 ns, corresponds to an impact parameter range of the order of the average space resolution.
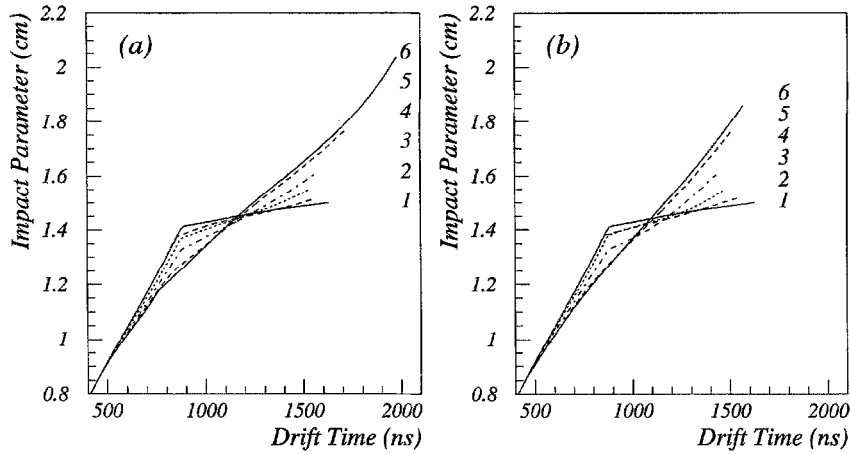
Fig. 7. Time to distance relations for all ϕ intervals. The plot (a) refers to the case $\beta_\ell < 0$, i.e. odd layers crossed at positive ϕ angles and even layers crossed at negative ϕ angles. The plot (b) refers to the complementary cases in which $\beta_\ell > 0$. The curves are labelled according to the numbering of the ϕ intervals defined in Table 1.
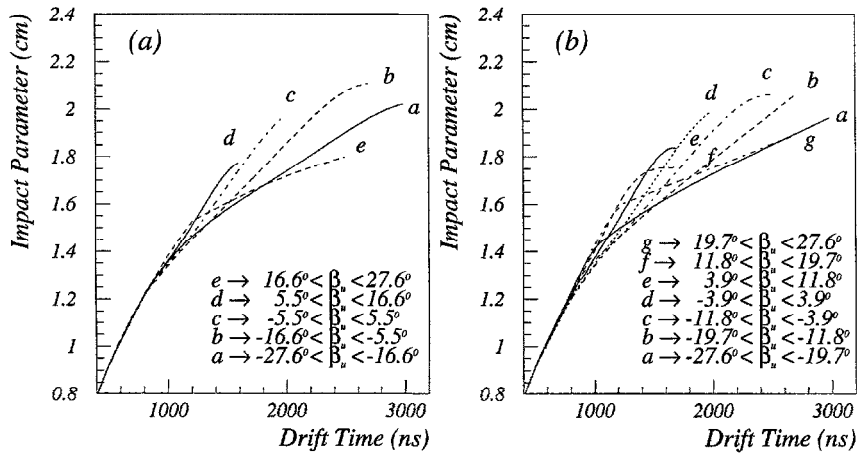

Fig. 8. Time to distance relations for five intervals of the β_u angle in the case $25° \leq \phi \leq 40°$ (a) and for seven β_u intervals in the case $40° \leq \phi \leq 50°$ (b).

larger than, or of the order of, half cell width ($w/2$) the fastest electrons come from the corner of the cell where the drift velocity is very low. The resulting effect on the relationship between resolution and drift time (averaged over all the crossed cells) is a decrease of the resolution in a wide time range which corresponds to a large average resolution in a very small impact parameter interval.

The resolution functions have been classified in the same ϕ, β_ℓ and β_u ranges described in Section 4.2. In Fig. 9 two sets of $\sigma(t_d)$ curves are plotted: the first one shows the dependence on ϕ and the second the dependence on β_u in the range $40° < \phi < 50°$.

The quantitative behavior of both $r(t_d)$ and $\sigma(t_d)$ are well confirmed by Monte-Carlo simulations of the cell response [18].

4.4. Fit to the resolution function

From the dependence of the spatial resolution on the impact parameter one can infer the numerical values of some of the parameters which characterize the used gas mixture.

Assuming that all contributions to the spatial resolution come exclusively from (a) primary ionization statistics; (b) electron diffusion in the gas; (c) intrinsic time resolution of the electronic setup; (d) interpolation error of the fitted track to the defined cell, one can fit the resolution function as the sum, in quadrature, of the described effects [19].

Table 1
Definition of the ϕ intervals for the study of the time to distance relations. $\langle\phi\rangle$ is the central value of the interval of width $\Delta\phi$

ϕ interval no.	$\langle\phi\rangle$	$\Delta\phi$	β_ℓ intervals	β_u intervals
1	0°	10°	1	1
2	8.75°	7.5°	2	3
3	15°	5°	2	5
4	21.25°	7.5°	2	5
5	32.5°	15°	2	5
6	45°	10°	2	7

Fig. 10 shows these fitted contributions (the range of impact parameter has been restricted to 1 cm only in order not to invade the field wire region delimiting the cell which presents the obvious singularities described in the previous paragraph). The primary ionization statistics has been parameterized as a function of λ, the mean-free path between two consecutive ionizing collisions ($\lambda = 1/n_p$, where n_p is the average number of primary ionizations per cm). The best fit gives $\lambda = (597 \pm 43)\,\mu$m corresponding to $n_p = (16.7 \pm 1.2)$ cm^{-1} for 50 GeV/c pions. This value is in very good agreement with Refs. [5,20,21] if one assumes an approximately 30% relativistic rise over the minimum ionizing value for helium. Analogous result is obtained from a fit to a Poissonian distribution, convoluted with the effects of the described processes, applied to different slices of the distribution of the arrival time of the first electron to the sense wire [19].

The contribution σ_D coming from the electron diffusion in the gas has been parameterized as the product of a term, which depends on the fraction n of the total ionization concurring to the arrival of the first electron on the sense wire, times the ratio of
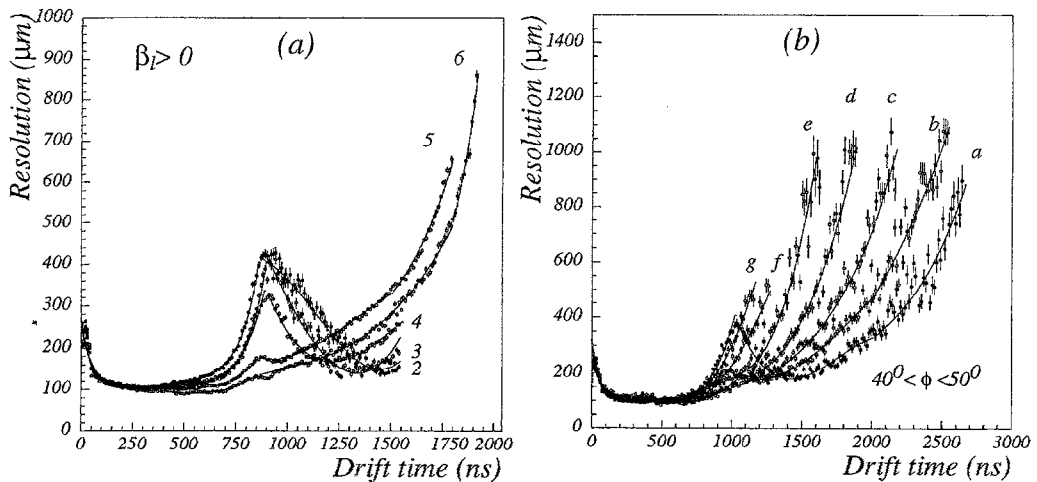

Fig. 9. Resolutions as a function of the drift time in the five ϕ slices corresponding to non-radial tracks (a), for hits falling in the inner-half of cells with $\beta_\ell > 0$ (curve labels according to Table 1). Resolution functions in the outer-half of the cell (b) for $\phi = 45 \pm 5°$ and different value of the β_u angle describing the cell deformation at the outer edge (the labels refer to the same β_u intervals as defined in Fig. 8b).
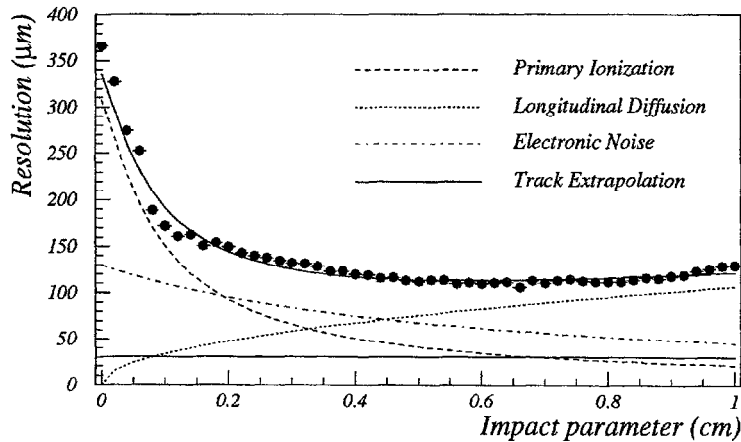
Fig. 10. Fit to the experimental resolution (dots) as the sum of the contributions from ionization statistics, electron diffusion, electronic noise and track extrapolation.

the diffusion coefficient $D(E)$ and the drift velocity $w(E)$ of the electrons in the gas [22]:

$$\sigma_D^2 = \frac{1.64}{2 \ln n} \frac{2D(E)}{W(E)} x, \tag{4}$$

x being the distance from the sense wire.

The best fit to the distribution in Fig. 10 gives

$$n = 9.57 \pm 0.13,$$

$$2\frac{D(E)}{w(E)} = (3.4 \pm 0.4) \times 10^{-4} \, \text{cm} \tag{5}$$

corresponding to $\sigma_D \sim 110 \, \mu\text{m}$ at 1 cm from the sense wire. This value is in perfect agreement with what one expects from the measurement of single-electron diffusion in the same gas mixture and for the same electric field [7].

The contribution due to the intrinsic time resolution of the electronic setup (constant in the time domain, is convoluted with the time to distance relations in the impact parameter domain) is due to the time jitter in the trigger and in the discriminated chamber signal, 1–2 ns, to the finite TDC resolution, of 1 ns, and to the channel by channel differences in the signal path. A fit to the resolution function of Fig. 10 gives $\sigma_t = (3.6 \pm 0.3)\,\text{ns}$, in agreement with what expected. The final contribution coming from the interpolation of the fitted

track, in the plot in Fig. 10, is $\sigma_{\text{interp.}} = (30 \pm 3)\,\mu\text{m}$ and is consistent with an average spatial resolution of $\sim 150 \, \mu\text{m}$ for tracks made, on average, of 25 layers.

5. Prototype performance

5.1. Efficiencies

The cell efficiency has been studied by looking for hits extrapolated from good-quality reconstructed tracks. The data used in this analysis were collected with an equivalent discrimination threshold of 4 mV corresponding to 1/4 of the signal produced by one electron. Results related to different cells have been put together, without cell by cell corrections, in order to get the average cell efficiency, shown in Fig. 11 as a function of the distance from the sense wire, in 1 mm wide bins of impact parameter.

The hardware efficiency, defined as the ratio of the number of hits in a cell over the number of tracks falling inside that cell, exceeds 99.7%. The corresponding inefficiency (0.0029 missing hits per track), shown in Fig. 12 as a function of the impact parameter, is in 48% of the cases localized at the edge of the cell and due to the cut of the drift times larger than 2 μs.
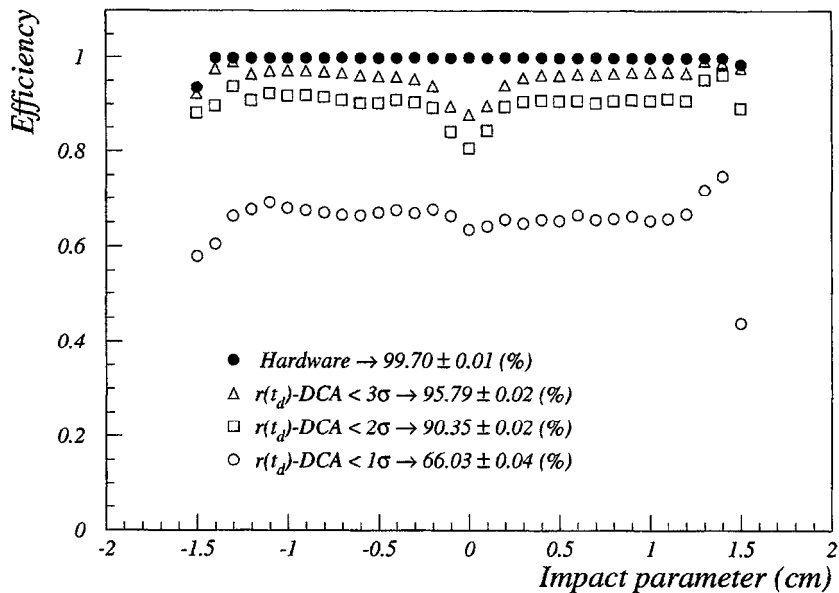
Fig. 11. Cell efficiency as a function of the distance (DCA) from the sense wire, for normally incident radial tracks.

In Fig. 11 the curves labelled as 1σ, 2σ and 3σ represent the fraction of events in which a hit is found at a distance from the extrapolated track, within 1, 2 or 3 times the value of the resolution function corresponding to the hit drift time. Therefore, they account for hardware efficiency, extrapolating power and level of knowledge of the calibration constant, i.e. of the $r(t_d)$ and $\sigma(t_d)$ functions.

The efficiency at 1σ is satisfactorily uniform within the cell and the average value of 66.03% entails a degree of knowledge of $r(t_d)$ and $\sigma(t_d)$ of better than 97.75%. A sensible drop of the efficiency is observed at 2 and 3σ in a region of impact parameters smaller than 0.3 cm, which originates from the non-Gaussian shape of the residue distributions, due to the low ionization density in helium.

In a similar way, one can also determine the level of noise in the chamber. An average noise occupancy of 0.002 noisy hits/(hit cell · event) is, in fact, measured by the number of hit cells at a distance from the track larger than w (gain of 10^5, threshold of 4 mV). No relevant correlations, like cross-talk, are observed.
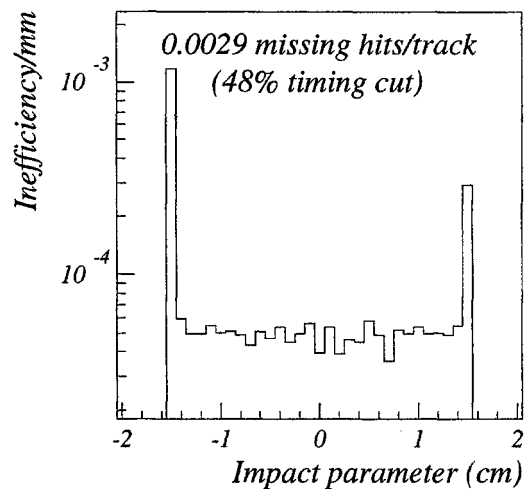

Fig. 12. Cell inefficiency as obtained from the same sample of tracks used in Fig. 11.

5.2. Spatial, momentum and angular resolutions

As shown in Figs. 6 and 9, the accurate studies of the time to distance relations and of the resolution

functions allow one to state that the chamber spatial resolution can be kept well below 120 μm over a considerable part of the drift cell, independent of its deformations due to the square shape and to the large stereo angles. They also allow us to extend the information from the drift time up to (99.85%) the physical width of the cell, without loss of efficiency and with only a moderate increment in spatial resolution.

Fig. 10 shows that all contributions to the spatial resolution are well understood. In reality, for the final chamber, the contribution due to the electronic setup will be negligible, whereas the one due to the track extrapolation does not apply. The effect of the magnetic field on the drifting of the electrons if, on the one hand, complicates the structure of the time to distance relations, on the other, it acts like an apparent expansion of the drift times. It is, therefore, not unrealistic to expect the final spatial resolution to be of the order of 100 μm for the large part of the drift cell [16].

Unfortunately, one will have to cope with the contribution due to the multiple scattering which will dominate, in the momentum resolution, despite the long radiation length of the gas mixture (~ 1300 m). Indicating with X_0 the gas radiation length, with B the magnetic field (0.6 T) and with N the number of track hits, one finds

$$\left(\frac{\Delta p_t}{p_t}\right)_{m.s.} = \frac{5.4 \times 10^{-2}}{B\rho\beta}\sqrt{\frac{\rho\sin\theta}{X_0}} = 1.9 \times 10^{-3}, \qquad (6)$$

$$\left(\frac{\Delta p_t}{p_t}\right)_{meas.} = \frac{8\sqrt{3}\sigma_x}{0.3B\;\rho^2\sqrt{N}}p_t = 0.75 \times 10^{-4} \qquad (7)$$

for an average KLOE track (of length in the transverse plane $\rho \sim 2$ m) traversing all 58 layers (without hitting any wires) with an average transverse momentum, p, of 200 MeV/c (and $p_t = p\sin\theta \sim 150$ MeV/c) and an average spatial resolution, σ_x, of 150 μm [23].

Fig. 13 shows the measured direction cosines of the beam ($\cos\alpha_x$, $\cos\alpha_z$) for normal incidence to the prototype ($\phi = 0°, \theta = 90°$ in the prototype rest frame). Given the negligible beam divergency, they give the angular resolution of the prototype: $\Delta\phi = 0.26$ mrad, $\Delta\theta = 2.25$ mrad. It is worth noting that they deviate from Gaussian distributions minimally, a further indication of the good knowledge of both time-to-distance relations and resolution functions.

The θ angular resolution, which is relevant for invariant mass resolution, will project, for the described average track in KLOE, to $\Delta\theta = 0.4$ mrad. Once again, the multiple Coulomb scattering

$$\Delta\theta_{m.s.} = \frac{13.6\,\text{MeV}/c}{\beta p}\sqrt{\frac{\rho}{X_0}} = 3.2\,\text{mrad} \qquad (8)$$

will dominate over the measurement.

Measurements of the direction cosines of the beam, for beam incidence different from normal, give values of $\Delta\phi$ and $\Delta\theta$ which are in good agreement (within 15%) with the ones for normal
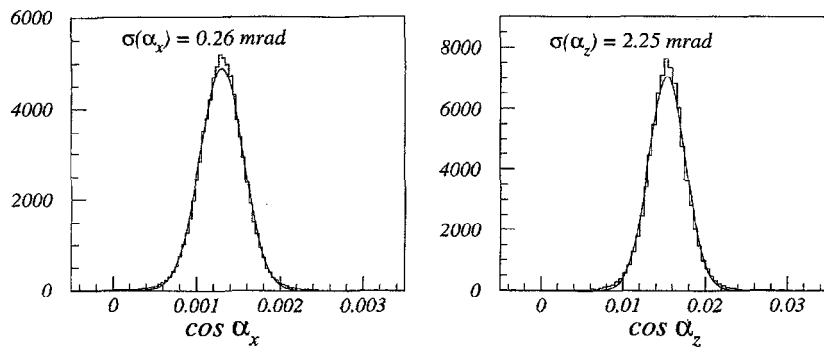

Fig. 13. Distributions of the x and z direction cosines of normal incidence tracks. The angular resolution of the detector is inferred from their width by assuming negligible beam divergency.
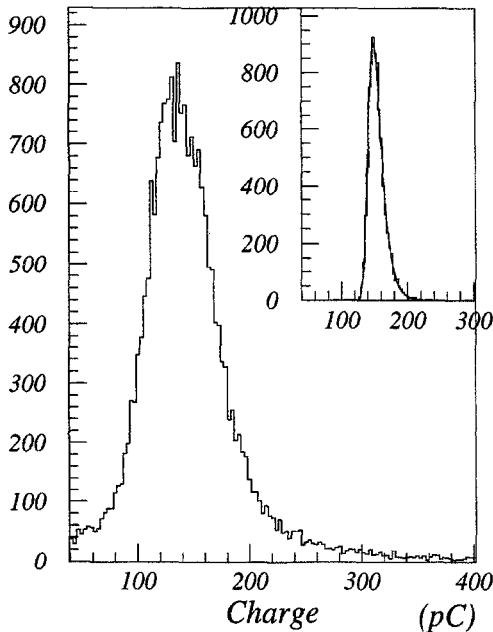
Fig. 14. Pedestal subtracted charge distribution of a $(3 \times \pi)\,\text{cm}^2$ drift cell. In the inset is shown the total charge summed over 50 different cells for a normal incidence track.

Fig. 15. dE/dx resolution as a function of the fraction of truncated hits. The cut at a value of 15% shows the best resolution and produces a Gaussian distribution.

incidence, if one takes into account the difference in track length and in number of hits on the track.

5.3. dE/dx resolution

Fig. 14 shows a typical charge spectrum, pedestal subtracted, of a $(3 \times \pi)\,\text{cm}^2$ cell for normal incidence tracks. The peak value is approximately 135 pC (FWHM of 60 pC), corresponding to an average gas gain of $(1.0 \pm 0.1) \times 10^5$. Excellent linearity has been verified for HV up to 2050 V and for track lengths up to 8 cm, corresponding to track θ angles down to about 20° with respect to the sense wire.

In order to study the behavior of the dE/dx resolution as a function of m, the number of samplings per track, different track segments have been summed together [24]. The inset in Fig. 14 shows the average charge, summed over 50 measurements for normal incidence tracks. The limited extension of the Landau fluctuations is a promising indica-
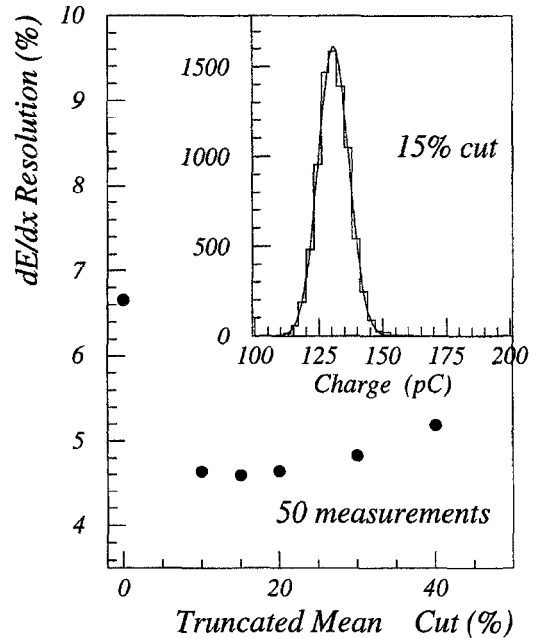
tion of the good quality of the gas mixture for dE/dx studies. Truncated means, with different fractions of the largest values, indicate that the best resolution (defined as the ratio of the width of the charge distribution over the peak value) is obtained with a cut of 15% as shown by the Gaussian behavior of the resulting distribution in the inset of Fig. 15.

The energy resolution after applying a 15% truncated mean cut, as a function of m, is shown in Fig. 16. The superimposed fit shows a clear $1/\sqrt{m}$ dependence $(m^\alpha, \alpha = -0.502 \pm 0.015)$ with a negligible constant term $(7.7 \pm 2.6) \times 10^{-3}$. The single measurement resolution is $(27.8 \pm 1.3)\%$. Assuming an average track length corresponding to approximately 80 hits in the KLOE chamber, in principle, one could get a dE/dx resolution of about 3.5%, which is an excellent result for a normal pressure gas device and could provide a relevant redundancy in the π/μ separation, for an efficient rejection of the $K_{\mu3}$ background to the $K_L \to \pi^+\pi^-$ decay.
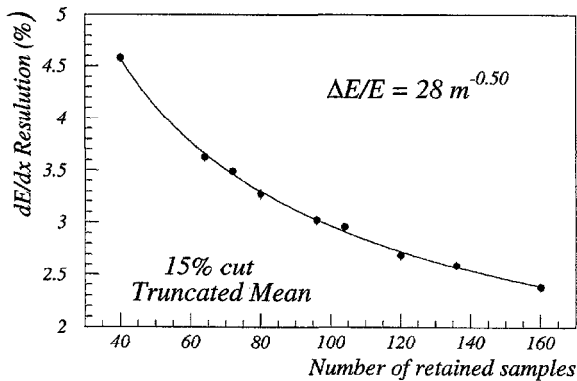
$$\Delta E/E = 28\, m^{-0.50}$$

Fig. 16. dE/dx resolution as a function of the number of used hits with a truncated mean cut of 15%. The superimposed fit shows the $1/\sqrt{m}$ dependence with negligible constant term and a single measurement resolution of about 28%.

6. Conclusions

A full-length prototype of the KLOE drift chamber has been built and successfully operated with a beam at CERN. The carbon fiber end plates were demonstrated to be fully compatible with all other materials chosen for the chamber. A little extra care is necessary only in removing leftover chips of carbon fiber from inside the feedthrough holes.

Helium tightness can be kept under control by properly sealing the feedthrough holes with a viscousless cyanoacrylic sealant. No difference, as far as electron transport properties in the gas, was found between the gas supplied to the chamber and the one purged from it, despite the large volume ($\sim 3\,m^3$), the large surface ($\sim 15\,m^2$) and the large number of wire feedthroughs (~ 4600).

Construction techniques like wire handling, wire transport, wire pulling and precisely tensioning, feedthrough crimping, proper ground soldering of field wires, preamplifier holding and power feeding, HV distributing and cable routing will be refined for the KLOE chamber assembly. The prototype has been safely transported from Lecce, where it was designed and built, to CERN and back (3200 km) without any damage.

From the detector point of view, one can conclude that the first sizeable drift chamber (500 sense

wires, 3.2 m long) in a helium-based gas mixture has been successfully operated in a beam test, since the first suggestion of helium as drift chamber gas for detectors at "factories" [23].

The particular full stereo geometry applied here has proven successful as far as efficiency and resolutions are concerned with a minor drawback on the complexity of the cell calibration and of the track-finding algorithm. Special care should be used in extending this algorithm to the case of bent tracks in magnetic fields.

A systematic study of the time to distance relations, as functions of the track angle in the cell and of the cell deformations due to the stereo angles, has been carried out, which allows us to utilize the drift information to the full extent of the drift cell, thus reaching an efficiency in excess of 99.85% with a negligible noise level. Spatial resolution of better than 120 μm has been reached over the large part of the cell, independent of the track angle, for all wires and without any wire by wire corrections. Its extent is fully understood in all its contributions. Angular resolution is perfectly consistent with the expected values given the spatial resolution and the stereo angles. A surprisingly good dE/dx resolution, of 28% on a single measurement, with a truncated mean of only 15% will allow, for an average track length in KLOE, an overall resolution of about 3.5%, which would be necessary for redundant rejection of the $K_{\mu 3}$ backgrounds to the CP-violating decay channels.

Acknowledgements

contributed to the full success of the prototype beam test.

References

[1] The KLOE Collaboration, KLOE, a general purpose detector for DAΦNE, LNF-92/019 (IR), 1992.

[2] The KLOE Collaboration, THE KLOE DETECTOR, Technical Proposal, LNF-93/002(IR); G. Finocchiaro for The KLOE Collaboration, Nucl. Instr. and Meth. A 360 (1995) 48; A. Calcaterra for The KLOE Collaboration, Nucl. Instr. and Meth. A 367 (1995) 104.

[3] A. Andryakov et al., Nucl. Instr. and Meth. A 379 (1996) 414.

[4] The KLOE Collaboration, The KLOE central drift chamber: Addendum to the KLOE technical proposal, LNF-94-028-IR, 1994.

[5] B. Schmidt, K. Martens, Nucl. Instr. and Meth. A 317 (1992) 148.

[6] P. Bernardini et al., Nucl. Instr. and Meth. A 355 (1995) 428.

[7] V. Golovatyuk, F. Grancagnolo, M. Primavera, Nucl. Instr. and Meth. A 394 (1997) 97; V. Golovatyuk, F. Grancagnolo, M. Primavera, KLOE memo no. 108, September 1997, unpublished.

[8] V. Golovatyuk, F. Grancagnolo, M. Primavera, KLOE memo no. 110, September 1997, unpublished.

[9] F. Grancagnolo for the KLOE Chamber Group, Nucl. Instr. and Meth. A 367 (1995) 108.

[10] S. Spagnolo for the KLOE Chamber Group, Nucl. Phys. B (Proc. Suppl.) 54B (1997)70; S. Spagnolo on behalf of the KLOE Tracking Group, Contribution to the "7th Pisa Meeting on Advanced Detectors", La Biodola, May 1997, Nucl. Instr. and Meth. A to be published. KLOE memo no. 93, Jun. 1997, unpublished.

[11] The end plates were fabricated by STESALIT, Zullwill, Switzerland.

[12] R.J. Yarema et al., A high performance multi-channel preamplifier ASIC IEEE Trans. Nucl. Sci. 30 (4) (1992).

[13] H. Beker et al., in; R. Shellard, T.D. Nguyen (Eds.), Proc. Computing in High Energy Physics, Rio de Janeiro, 1995, World Scientific, River Edge, NJ, 1996.

[14] J.K. Ousterhout, Tcl and Tk toolkit, Addison-Wesley, Reading, MA, 1994.

[15] D. Picca, La camera centrale dell'esperimento KLOE sulla violazione di CP: studio di prototipi e misura della tensione meccanica dei fili, Tesi di Laurea, Università di Roma, "La Sapienza" A.A. 1994–1995, unpublished.

[16] F. Lacava for the KLOE Chamber Group, Nucl. Phys. B (Proc. Suppl.) 54B (1997) 327. The whole set of measurements obtained with this prototype is going to be presented in a forthcoming paper.

[17] G. Cataldi et al., Nucl. Instr. and Meth. A 388 (1997) 127–134; M. Primavera, S. Spagnolo, KLOE note 153, December 1995.

[18] The cell response has been studied in many configurations by means of the drift chamber simulation package GARFIELD, R. Veenhof, GARFIELD a drift chamber simulation program – Version 3, 1991; CERN Program Library W5050; P. de Simone, KLOE memo no. 35, Sepetember 1995, unpublished; P. de Simone, KLOE memo no. 76, December 1996, unpublished.

[19] C. Luisi, KLOE memo no. 78 (unpublished); C. Luisi, L'esperimento KLOE a DAΦNE. Studio delle caratteristiche della cella e della miscela elio-isobutano per la camera a deriva centrale, Tesi di Laurea, Università di Roma, "La Sapienza" A.A. 1994–1995, unpublished.

[20] A. Sharma, F. Sauli, Nucl. Instr. and Meth. A 350 (1994) 470.

[21] G. Cataldi, F. Grancagnolo, S. Spagnolo, Nucl. Instr. and Meth. A 386 (1997) 469.

[22] V. Palladino, B. Saudoulet, Nucl. Instr. and Meth. A 128 (1975) 323.

[23] F. Grancagnolo, in: E. DeSanctis, M. Greco, M. Piccolo, S. Tazzari (Eds.), Proc. Workshop on Heavy quarks factory and nuclear physics facility with Superconducting Linacs, Courmayeur, 1987, p. 599; F. Grancagnolo, Nucl. Instr. and Meth. A 277 (1989) 110.

[24] E. De Lucia, KLOE memo no. 79 (unpublished); E. De Lucia, Misura della ionizzazione specifica in prototipi della camera a deriva dell'esperimento KLOE, Tesi di Laurea, Università di Roma, "La Sapienza" A.A. 1995–1996, unpublished.